# Characteristic of short-range exposure to cough-produced vortex rings under different mouth shapes and velocities using large eddy simulation

*Kaijun* Li[1*], *Ruibin* Li[1], *Lingjun* Xiao[1], *Naiping* Gao[1], and *Yan* Wu[1]

[1]School of Mechanical Engineering, Tongji University, Shanghai, 201804, China

**Abstract.** Coughing is one of the major routes for the transmission of respiratory diseases in indoor environments. Previous studies have shown that coughing can form vortex ring structures. However, the conditions under which cough-generated vortex rings form, as well as the influence of boundary condition on the formation and flow characteristics of these vortex rings, remain inadequately understood. This study investigates the effects of three velocity profiles (real-cough, sinusoidal, and pulsation) and five outlet shapes (real-mouth, circular, square, rectangular, and elliptical) on the flow dynamics of cough jets. The results show that the penetration distance of cough-generated vortex rings ranges from 0.56 to 0.68m in 0.5s. Separated (or deviated) vortex rings show a power-law distribution in the cough jets: $s \sim t^{2/3}$ (or $s \sim t^{1/2}$) during the initial stage and $s \sim t^{1/3}$ (or $s \sim t^{1/5}$) during the interrupted stage. Due to the differences between the power-law and existing studies, short-distance infection risk assessment models require further revision. Furthermore, the real-mouth, circular, and square have a relatively minor effect on the formation of saturated vortex ring compared to velocity profiles. The formation conditions for saturated vortex rings can be determined by a dimensionless energy $\alpha_{\text{lim}} = 0.2 \pm 0.06$.

## 1 Introduction

Respiratory infections such as COVID-19 can spread through contact, droplets, and aerosols [1]. Controlling droplet transmission is vital for public health and sustainable development. Studies emphasize the role of short-range airborne transmission, especially since maintaining 1.8-4 m distance is challenging in daily life [2]. Coughing, a key respiratory event, significantly contributes to short-range indoor transmission and has been widely studied [3]. While transmission depends on pathogen characteristics, fluid dynamics are crucial. Research using LES [4], Schlieren imaging [5], and DNS [6] reveals that coughing generates vortex rings that enhance droplet transport. Per Helmholtz theory, these rings are stable, resist disturbances, and enable long-distance dispersion [7]错误!未找到引用源。. Thus, cough jet dynamics critically affect short-range disease spread. Understanding their flow behaviour in the first few seconds is essential, as this stage governs exposure risks between nearby individuals [8].

A real cough flow rate can be described by a gamma probability distribution function, with a duration ranging from 0.1 to 0.5 s and a peak velocity between 6 and 28 m/s [9]. Cough jets generally exhibit two stages: a starting jet and an interrupted jet [10]. To simplify modelling, many studies use idealized pulsating or sinusoidal profiles [11-13]. Real and sinusoidal profiles often show better penetration than pulsatile ones under similar Reynolds numbers (Re) [10]. Behera et al. [14] reported that real cough jets can travel ~1.1 m in 0.5s. Several studies have shown that cough jets typically feature leading vortex rings followed by trailing jets, which significantly influence droplet transport distances [15-16]. Droplets smaller than 1 μm are mostly entrained within these structures [4]. The separated vortex rings move faster than the main puff body and play a dominant role in cough flow dynamics [17]. These rings, especially in male subjects, propagate faster than the puff and are influenced by the cough velocity profile and outlet shape [17-18].

In computational studies, the mouth is typically simplified as a circular, rectangular, or elliptical outlet [11]. As cough flow behaves like a starting jet [10], fluid mechanics suggests that outlet geometry significantly affects vortex ring formation and evolution [19-20]. Additionally, the outlet geometry influences the formation number ($F$), which marks the transition from a single vortex ring to one followed by a trailing jet. In piston-cylinder setups, $F$ is about 4 [21], while rectangular outlets yield values between 1.5 and 2.3 depending on aspect ratio [22]. Thus, investigating cough jet dynamics in relation to mouth shape is crucial for accurately modelling airflow and understanding pathogen transmission.

In summary, both the mouth opening shape and the velocity profile of cough jets play critical roles in determining flow penetration, droplet transport, and vortex ring structures. However, most existing studies rely on simplified assumptions, such as pulsating velocity profiles and circular outlets, without fully reflecting real cough dynamics. Moreover, there is a lack of research on vortex ring formation numbers in human coughs and the factors influencing vorticity strength under various boundary conditions. To address these gaps, this study investigates the coupled effects of mouth shape and velocity profile on the temporal evolution of cough jet dynamics using large eddy simulation (LES).

## 2 Introduction

The three-dimensional computational domain, with dimensions of 0.6 m × 0.6 m × 1.5 m, is shown in Fig. 1(a). To assess the impact of mouth geometry, five inlet shapes were modelled: real-mouth, circular, square, rectangular, and elliptical (Fig. 1(b)), each with an area of 4 cm$^2$. The equivalent diameter is calculated by ${D_{eq}}^2 = 4 \times \frac{A_p}{\pi}$. Large Eddy Simulation (LES) was chosen for its balance between accuracy and computational cost. The WALE model [23] was used for subgrid-scale turbulence, offering good performance in respiratory flow simulations compared to the more expensive dynamic Smagorinsky model [24]. The pressure-velocity coupling was handled using the SIMPLE solver. The spatial discretization of the momentum equations employed the bounded central difference scheme, while pressure interpolation used a second-order scheme. Temporal discretization was based on the bounded second-order implicit scheme. An adaptive time step size was used to maintain a Courant number (CFL) = 0.9 for all grid settings. As a result, the time step varied throughout the entire calculation process. During the cough jet exhalation phase, the time step was usually set to $1\times10^{-5}$ seconds to accurately resolve the transient behaviour. To study aerosol transport, $CO_2$ was used as a tracer gas, following previous studies [25-27], with a cough-emitted concentration of 40000 ppm [28]. Tracer gas transport equations used bounded central differencing for spatial discretization

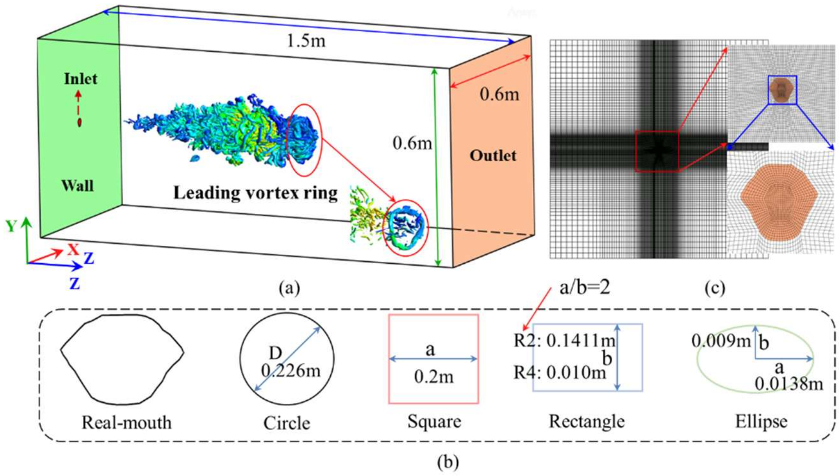


**Fig. 1** (a) The three-dimensional geometric model for cough jets. The origin point is located at the centre of the inlet; (b) Five mouth shapes for cough jets; (c) Real mouth-shaped fluid domain mesh.

Three distinct cough jet profiles are generated by varying the inlet velocity conditions: real-cough, sinusoidal and pulsating programs, as shown in Fig. 2. The corresponding Reynolds number ($Re = U_c D_{eq}/\nu$) is 7520. The duration of the cough jet is set to 0.2 s, with an expiratory volume of 400 ml. The release direction of the cough jet is perpendicular to the inlet plane. The temperature of the cough jet was not considered in this study for simplicity based on previous studies foundation [29-30].

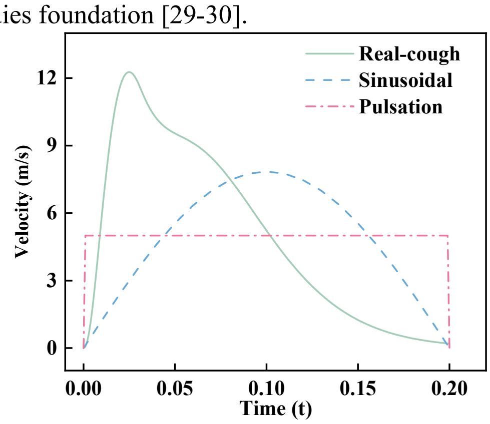


**Fig. 2** Three velocity profiles at the outlet in this study.

## 3 Results and discussion

### 3.1 Visualization of cough flow

The cough flows under different outlet shapes and velocity profiles are visualized using the mass fraction distribution of air exhaled by coughing to observe the formation and development process of vortex rings. The temporal evolution of cough jet with various outlet shapes under the real-cough velocity profile is shown in Fig. 3. As can be seen in Fig. 3(a), the velocity distribution and vortex structure of the cough jets are similar to those of vortex rings produced using a piston/cylinder configuration. Therefore, cough jets can generate leading vortex rings at the front of the cough cloud. These vortex rings can be clearly observed in all mouth shapes, as shown in Fig. 3(a). For non-axisymmetric outlet shapes with longer major axes (R2 and R4), drastic axis switching can cause the vortex ring structure to break up earlier. In other words, the formed vortex ring is broken by the jet source at $t^*$=0.20, as shown in Fig. 3(b). In contrast, the vortex rings formed in the other outlet configurations gradually dissipate, with the real-mouth shape maintaining the most coherent structure over time, as shown in Fig. 3(b) and (c). These vortex rings may contribute to the increased complexity of cough transmission to some extent and may result in the spread of respiratory pathogens over greater distances, which differs from the behaviour observed in traditional, steady-state circular jets. The vortex ring travelled more than 26 times the equivalent diameter $D_{eq}$ (about 0.58 m) for a real-cough with a real-mouth, potentially impacting the short-range transmission mode of respiratory droplets. As time goes on, the vortex ring formed by the cough jet will gradually dissipate and transform into a "puff" shape. Additionally, as shown in Fig. 3(b) and Fig. 3(c), the airflow distribution from the real-mouth outlet exhibits greater asymmetry and complexity due to the irregular geometry of the mouth opening. This observation is consistent with the findings of Wang et al. [31]. In comparison, the circular, elliptical, rectangular, and square outlets exhibit more symmetric airflow expansion with relatively weaker turbulent effects.

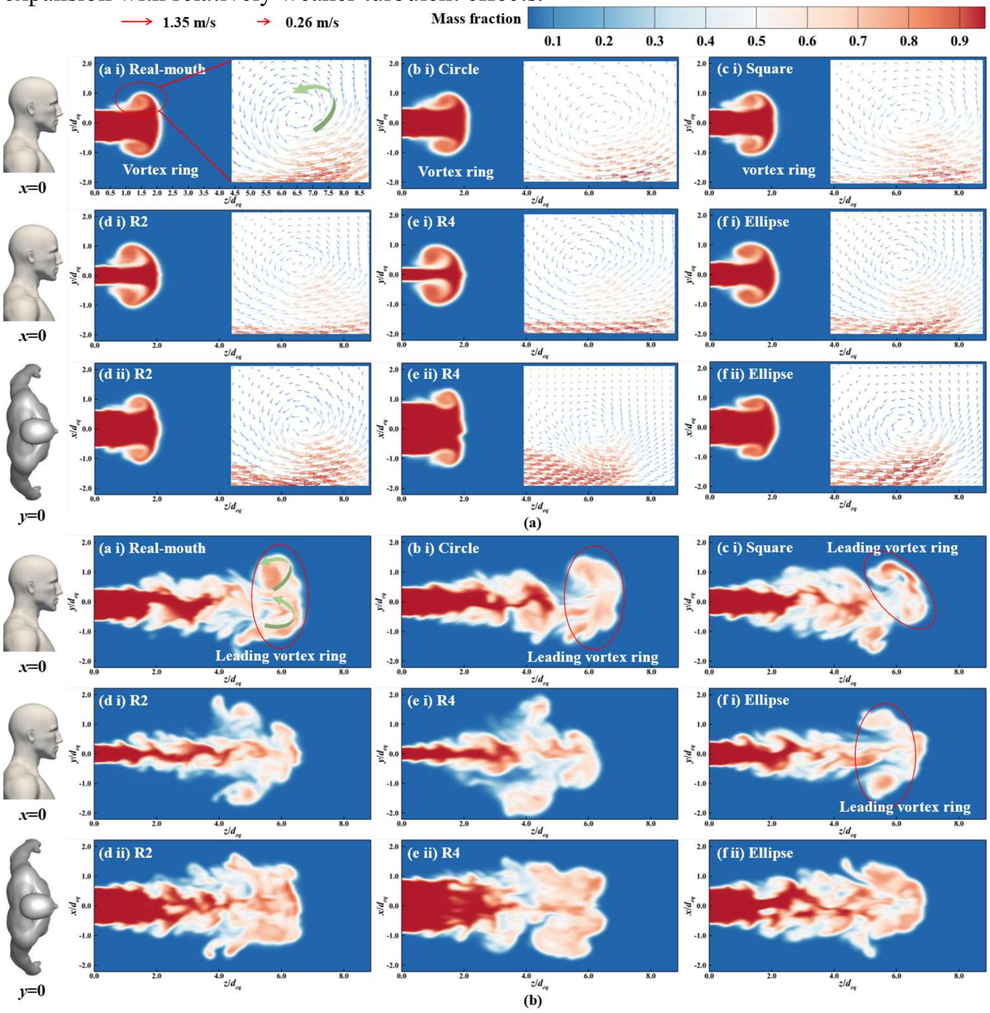

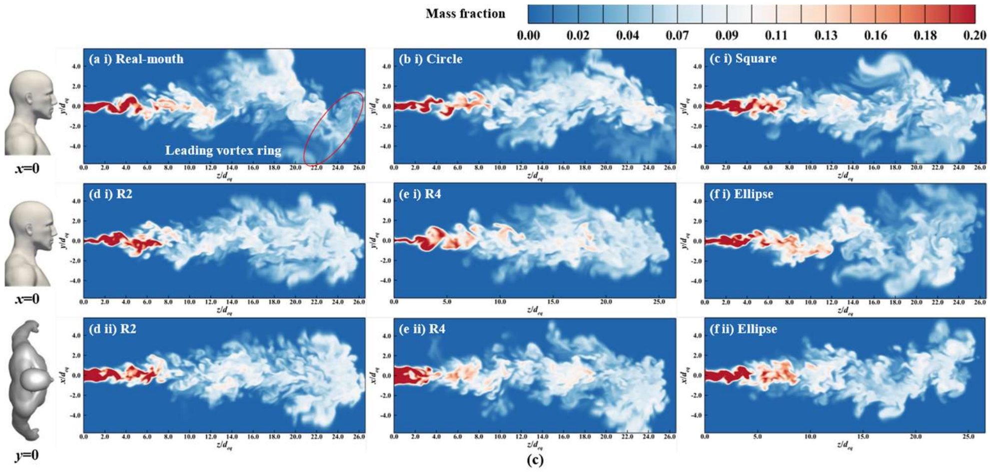

**Fig. 3** Visualizations of cough flow with different outlet shapes under the real-cough at $t = 0.02$ s ($t^* = t/t_c = 0.10$). (d i), (e i) and (f i) represent the minor axis plane (x = 0 m) for rectangular (R2 and R4) and elliptical outlet shapes, respectively; (d ii), (e ii) and (f ii) represent the major axis plane (y = 0 m) for rectangular (R2 and R4) and elliptical outlet shapes, respectively. The subplot shows the vortex ring velocity vector diagram.

Fig. 4 shows the temporal evolution of cough jets under different velocity profiles with the real-mouth outlet shape. As shown in Fig. 4(a i), (b i) and (c i), vortex rings are formed and develop in all three cases. In fact, any unsteady jet flow can generate vortex rings or vortex-like flow structures due to the rolling-up of the shear layer, as shown in Fig. 3(a) and Fig. 4. During the cough jet stage ($t^* \leqslant 1$), the real-cough profile produces the longest penetration distance, with vortex rings propagating the farthest. In contrast, the pulsating jet exhibits the shortest penetration and the most rapid breakdown of vortex rings, as shown in Fig. 4(a ii), (b ii) and (c ii). This indicates that the real-cough velocity profile provides higher momentum, enabling the jet to travel further. The total momentum of the real-cough jet and sinusoidal jet is 64% and 23% higher than that of the pulsed jet, respectively. Additionally, it is notable that the pulsating jet shows no residual airflow near the outlet, as shown in Fig. 4(a iii), (b iii), and (c iii). The probable reason is that, compared to pulsed jets, real cough and sinusoidal jets have a relatively gentle change in velocity. The lower velocity is insufficient to catch up with the trailing jet stream in front of it.

The formation and development of vortex rings produced by coughing are directly influenced by the shape of the mouth. The irregular geometry of the real-mouth outlet leads to asymmetry in the cough jet and enhances its radial diffusion. In addition, the velocity profiles of the cough jet affect its penetration distance. The pulsed jet causes the leading vortex rings to break up earlier (Fig. 4(c iii)). Furthermore, the vortex rings generated by the real-mouth shape can travel distances exceeding 26 times the equivalent diameter $D_{eq}$ (0.6 m), as shown in Fig. 6. The vortex rings generated by coughing change the flow trajectory of conventional pulsed jets, affecting the motion and evaporation of droplets, and potentially altering short-range respiratory diseases transmission risk.

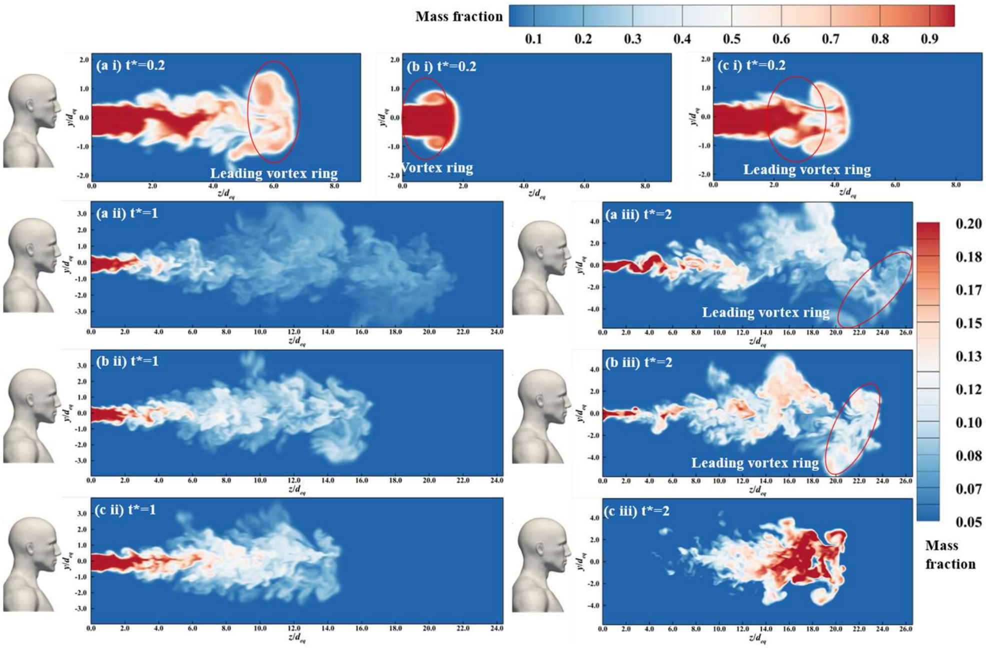


**Fig. 4** Visualizations of cough flow with different velocity profiles using the real-mouth outlet shape ($t^* = t/t_c$). (a i), (a ii) and (a iii) represent the real-cough velocity profile; (b i), (b ii) and (b iii) represent the sinusoidal velocity profile; (c i), (c ii) and (c iii) represent the velocity profile of the pulsation.

## 3.2 Cough jet penetration distance Formatting the title, authors and affiliations

Following the qualitative analysis of cough jet behaviour, more detailed quantitative investigations were conducted. Fig. 5 shows the streamwise dimensionless penetration distance ($z/D_{eq}$) of the cough jet as a function of dimensionless time ($t^* = t/t_c$). The penetration distance as the point at which the wavefront velocity drops to within the range of 0.05-0.10 m/s [5]. As shown in Fig. 5, when $t^* = 10$ ($t = 2$ s), the penetration distance of the cough jet reaches 35-45$D_{eq}$, corresponding to 0.79m to 1.02m. During the first 0.4 s ($t^* = 2$), the cough jet travels a relatively long distance, about 25-30$D_{eq}$ (0.56-0.68 m). However, it took much longer to cover the remaining distance. Furthermore, during the starting jet stage ($t^* \leq 1$), the penetration distance is nearly identical across different outlet shapes, suggesting that outlet geometry has minimal influence at this stage. This is because the cough jet is in the self- preserving region of unsteady turbulence, which is consistent with previous studies showing self-preserving behaviour at distances greater than 20 to 30 outlet diameters [32]. Within this region, the maximum streamwise penetration distance with time can be expressed as Eq. (1), which is applicable to both situations in Fig. 5.

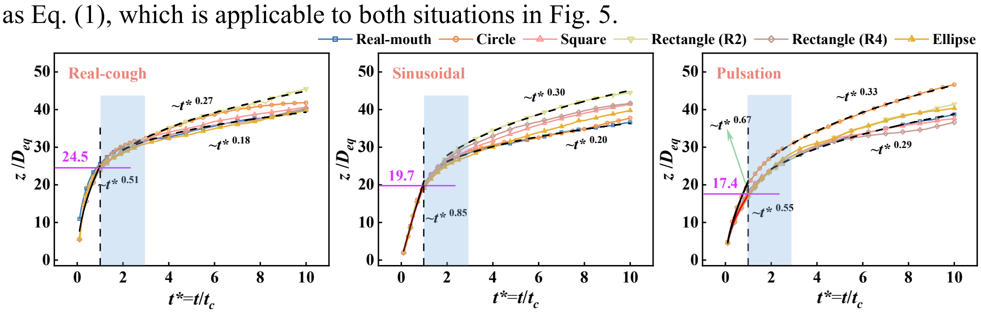

**Fig. 5** Dimensionless penetration distance when the velocity decreases to 0.05-0.1 m/s.

$$\frac{z}{D_{eq}} \approx A_d \left(\frac{t}{t_c}\right)^{-B_d} \quad (t \leq t_c) \tag{1}$$

where, $A_d$ is the penetration distance when $t^* = 1$. $B_d$ is a constant and is related to the velocity programs.

In the interrupted jet stage ($t^* > 1$), the outlet shape has a more significant impact on penetration distance than the velocity profiles. The jet penetration distance of the real-mouth is lower than that of other shapes. This is due to the irregular shape of the real-mouth, which induces increased radial diffusion, as shown in Fig. 3. As can also be seen from Fig. 5, when considering the social distance to prevent short-range droplet transmission, the outlet shape can be simplified to a rectangle (R4) or an ellipse to build a model for real-cough jets; the outlet can be simplified to a circle for sinusoidal cough jets; the outlet can be simplified to a square for pulsating cough jets. Additionally, in this study, different from the previous studies, the penetration distance as a function of time follows a scaling law of $t^{1/2}$ for the starting jet stages and $t^{1/4}$ for the interrupted jet phase.

When $t^* < 1$, mouth shape has little effect on jet penetration distance. The normalized streamwise penetration distances ($s$) follows a self-similarity relation: $s \sim t^{0.51}$, consistent with previous studies [9, 10, 33]. When $t^* > 1$, the results with real-mouth show $s \sim t^{0.20}$ for real-cough and sinusoidal profiles, and $s \sim t^{0.33}$ for pulsation profile. However, the experimental results of Wang et al. [31], Bourouiba et al. [9] and Wei et al. [10] reported exponents of 0.30 and 0.25, respectively. Wang et al. [33] indicated that the exponent for circular outlets with real-cough-like profiles decreased from 0.33 to 0.27, aligning with this study's trends (Fig. 5). The discrepancies can be explained as follows: (1) This study defines penetration distance as the projected front along the z-axis, not along the jet centerline [9]; (2) The real-mouth shape introduces radial diffusion and asymmetry, leading to faster decay in real-cough and sinusoidal cases (Fig. 3, Fig. 5). In the case of pulsed jets, the leading vortices are less affected by the irregular shape and can maintain their motion along the z-axis rather than deflecting downwards, as shown in Fig. 4. (3) In fact, no two coughs that are the same. The actual conditions of the individuals tested may differ from the parameters used in the simulation; (4) Wei et al. [10] employed a piston-cylinder apparatus to generate the cough jets, which can alter vortex ring formation. Therefore, the motions of the leading vortex and trailing jet differs from that reported in previous research after the end of the cough jet.

For circular impulse jets, the relationship follows $s \sim t^{0.67}$ ($t^* < 1$), and $s \sim t^{0.33}$ ($t^* > 1$), indicating faster penetration than other shapes, as shown in Fig. 5. This is attributed to the clean separation of circular vortex rings from the trailing jet (Fig. 6). Compared to the trailing jet, the separated vortex rings resulting self-contained structure move faster and can travel large distances [15]. Additionally, Johnson [34] also experimentally demonstrated that the distance travelled by the vortex ring as a function of time was $s \sim t^{2/3}$ ($t^* < 1$), which is consistent with the present study.

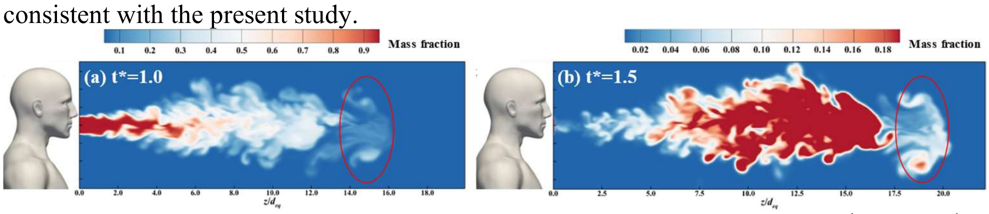


**Fig. 6** Visualizations of cough flow with circular outlet shapes for the pulsation jet. (a) $t^*$=1.0; (b) $t^*$= 1.5.

### 3.3 Saturated vortex ring of the cough jet

As shown in Fig. 3 and Fig. 4, coughing jets generate vortex rings within the flow structure. The vortex ring grows by absorbing the vorticity from the source and eventually reaches a limiting value (i.e., the saturated vortex ring, as shown in Fig. 3). To further analyse the conditions for saturated vortex ring formation in the human cough jet, this section discusses the effect of the outlet shapes and velocity profiles on three key aspects: the total circulation, formation number of vortex rings, and the streamwise position of these vortex rings (Related concepts can reference the literature [21]). The method of Gharib et al. [21] is used to determine the formation number (*F*). The formation number can be determined as the dimensionless formation time ($\frac{Ut}{D_{eq}}$) at which the total circulation of the discharged flow is equal to the circulation of the pinch-off vortex ring. The "formation time" refers to subsequently corresponds to the dimensionless formation time. Fig. 7 shows the effect of different outlet shapes and velocity profiles on the total circulation and circulation of the vortex ring.

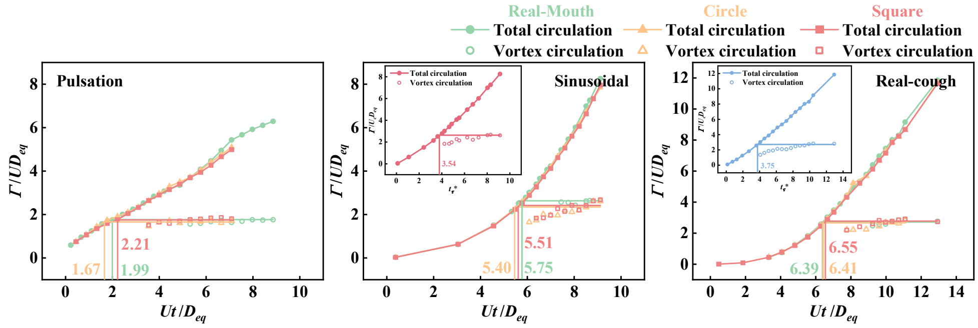


(a)

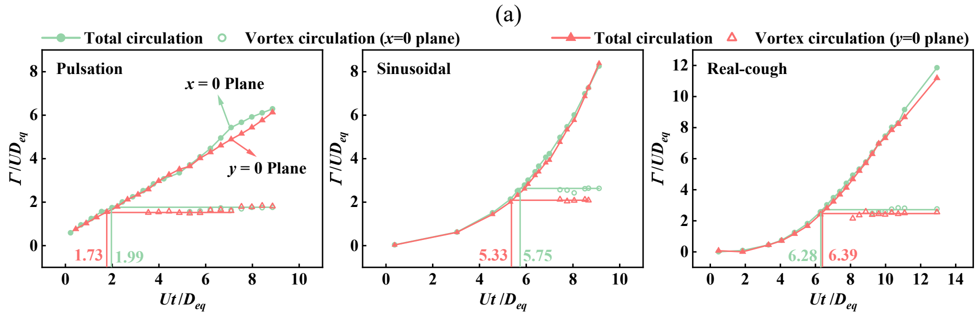


(b)

**Fig. 7** Dimensionless circulation of vortex rings as a function of formation time ($Ut/D_{eq}$). (a) x=0 plane. The subplot is dimensionless circulation of vortex rings as a function of formation time ($\int_0^t u(\tau)d\tau/D_{eq}$); (b) Dimensionless circulation of vortex rings with different planes for real-mouth outlet. U is the average velocity at which the continuous jet phase of the complete vortex ring can be observed.

It can be observed from Fig. 7(a) that the outlet shapes have little effect on the formation number of vortex rings compared to the velocity profiles. The dimensionless circulation of the vortex ring is approximately 1.71 for pulsation jets, 2.46 for sinusoidal jets, and 2.73 for real-cough jets, respectively. The range of formation numbers is 1.95±0.28 for pulsation, 5.55±0.20 for sinusoid, and 6.45±0.10 for real-cough, respectively. Fig. 7(b) shows the dimensionless circulation of different cross sections as a function of formation time for real-mouth. It can be observed that the formation number of vortex rings for different cross sections is almost the same. Furthermore, the total circulation exhibits an almost linear increase with $\frac{Ut}{D_{eq}}$ for impulsive cough jets. However, the total circulation is correlated with the square of $\frac{Ut}{D_{eq}}$ for sinusoidal and real-cough jets. In the initial stage of the jet, the total circulation increases slowly with $\frac{Ut}{D_{eq}}$, resulting in higher formation numbers. Moreover, an interesting phenomenon was found when the definition of the formation time on the horizontal axis of Fig. 7(a) is changed to $t_\tau{}^* = \frac{\int_0^t u(\tau)d\tau}{D_{eq}}$ (where $t$ is the physical time from the beginning of the cough jets), the total circulation is linearly related to the formation time $t_\tau{}^*$, as shown in Fig. 7(a). The formation number becomes 3.54 and 3.75 for sinusoidal and real-cough jets, respectively. Zhu et al. [35] found that when using $t_\tau{}^*$ to determine the formation number of the sinusoidal velocity program, the obtained value was 3.5. Therefore, the formation number alone is insufficient as a criterion for determining whether saturated vortex rings are formed. The determination of the formation number depends on the definition of the formation time. Consequently, further analysis is needed to identify the conditions for the formation of cough saturated vortex rings.

The three invariants (i.e., the kinetic energy $E$, circulation $\Gamma$, and impulse $I$), which characterize the properties of the vortex ring, can be calculated using Eq. (2-4) [36].

$$E=\rho\pi\iint\left(v^2+w^2\right)ydzdy \quad (2)$$

$$\Gamma=\int\omega dzdy \quad (3)$$

$$I=\rho\pi\iint\omega y^2 dzdy \quad (4)$$

where, $\rho$ is the fluid density, kg/m$^3$; $\omega$ is vorticity, s$^{-1}$; $v$ and $w$ is the fluid velocity, m/s. The dimensionless energy $\alpha_{cough}$ is defined by Eq. (5) [21].

$$\alpha_{\text{cough}}(t)=\frac{E}{\rho^{1/2}I^{1/2}\Gamma^{3/2}} \quad (5)$$

Fig. 8 shows the non-dimensional energy $\alpha_{cough}$ as a function of the two formation times. When the dimensionless parameter $\alpha_{cough}(t) < \alpha_{lim}$, the vortex rings will either absorb vorticity or not accept any new vorticity from source [21]. Therefore, $\alpha_{lim}$ represents the dimensionless energy corresponding to the saturated vortex ring (formation number). The results indicate that the limiting value of the nondimensional energy for saturated vortex rings falls within the range of 0.23±0.03 for the pulsatile and sinusoidal velocity programs. However, in the real-cough, the value of $\alpha_{lim}$ dropped to 0.14. The sinusoidal and real-cough velocity programs show a rapid decay compared to the slow decay tendency of the pulsed jet. Moreover, different definitions of formation times result in different formation numbers of vortex rings. To determine the conditions for saturated vortex ring formation, the variation of the dimensionless energy $\alpha_{coug}$ with different definitions of formation times is shown in Fig. 8. The results show that the determination of $\alpha_{lim}$ is independent of the definition of the formation time and can be used as a basis for the identifying of the saturated cough vortex ring.

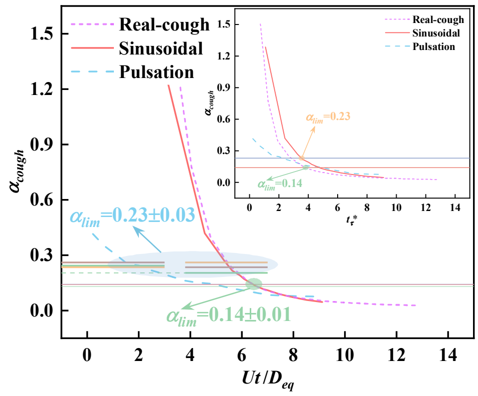


**Fig. 8** Non-dimensional energy $\alpha_{cough}$ with formation time ($Ut/D_{eq}$). The subplot shows the variation of the dimensionless energy with the formation time ( $\int_0^t u(\tau)d\tau/D_{eq}$);

Compared to the formation number, which is defined based on the dimensionless formation time, the dimensionless energy $\alpha_{lim}$ is a more general parameter for determining the formation of saturated vortex rings produced by coughing. The nondimensional energy $\alpha_{lim}$ decreased to about 0.20±0.06 for three velocity profiles (Fig. 8), which is consistent with the range of about 0.15-0.22 reported by Yu et al. [37]. Compared to the results (about 0.33) reported by Gharib et al. [21], the lower $\alpha_{lim}$ may also be partly attributed to the method adopted for calculating the circulation of vortex rings [38]. The primary vortex contains a large amount of non-rotating fluid, which influences the energy level, and the vortex ring does not contact with the axis, as shown in Fig. 4. When calculating the circulation of the leading vortex ring, only the rotational fluid was considered [38]. However, the dimensionless energy $\alpha_{cough}$, which includes the irrotational fluids would increase the value of the kinetic energy $E$. Additionally, the value of $\alpha_{lim}$ for the real cough jet is slightly lower than that for the sinusoidal jet, with a decline from 0.24 to 0.14. This can be attributed to the fact that the total impulse increases with increasing $Ut/D_{eq}$ [39]. Therefore, the real-cough jet has a larger formation number compared to the sinusoidal jet.

## 4 Conclusion

This study investigates the propagation behavior of various cough jets under different outlet shapes and velocity profiles, with a focus on their effects on penetration distance, entrainment volume, and formation conditions for saturated vortex ring. The main conclusions are as follows:

(1) Compared to outlet shapes, velocity profiles have a greater influence on penetration distance and the emergence of separating vortex ring. The real-cough velocity profile is adaptable to simplified outlet shapes. For the same *Re* and cough exhaust volume, vortex rings for real-cough jets in the starting jet stage shows stronger penetration capability, reaching 0.5-0.6 m, compared to sinusoidal and pulsating profiles.

(2) All unsteady jet flows can potentially generate vortex rings or vortex-like structures. The short-distance propagation of cough jets can be divided into two stages: the vortex ring propagation stage and the dispersive propagation stage. The vortex rings generated by cough jets alter transient flow behaviour. For a circular opening with a pulsed cough jet, the relationships between penetration distance and time are $s \sim t^{2/3}$ ($t^*$<1) and $s \sim t^{1/3}$ ($t^* \geqslant 1$) for the vortex ring propagation stage due to the vortex ring separation phenomenon. The irregular outlet shape of real-mouth causes vortex rings to deviate from the main jet direction. The

relationship between penetration distance and time is $s \sim t^{1/2}$ ($t^*$<1) in the vortex ring propagation stage, and $s \sim t^{1/5}$ ($t^* \geqslant 3$) in the dispersive propagation stage for sinusoidal and real-cough jets. These findings suggest that coughing should be modelled as a starting jet rather than a steady jet.

(3) The leading vortex ring generated during a cough initially grows by absorbing vorticity from the source and eventually reaches a saturation state, forming a saturated vortex ring. The effect of different outlet shapes (real-mouth, circle and square) on the formation number of vortex rings is negligible. The formation numbers determined by the formation time defined by the average velocity are 1.95 for pulsating, 5.55 for sinusoidal, and 6.45 for real-cough jets, respectively. The formation condition for the saturated vortex ring can be determined by the dimensionless energy $\alpha_{lim} \approx 0.20 \pm 0.06$.

**Acknowledgements**
This work was supported by the National Natural Science Foundation of China under the project number of 52378105.

## References

1. Zhang, R., Li, Y., Zhang, A. L., Wang, Y., & Molina, M. J. (2020). Identifying airborne transmission as the dominant route for the spread of COVID-19. Proceedings of the National Academy of Sciences, 117(26), 14857-14863. https://doi.org/10.1073/pnas.2009637117
2. Wang, C., Xu, J., Zhai, H., So, L. K., & Guo, H. (2025). Mapping full-range infection transmission from speaking, coughing, and sneezing in indoor environments and its impact on social distancing. Journal of hazardous materials, 490, 137782. https://doi.org/10.1016/j.jhazmat.2025.137782
3. Duguid, J. P. (1946). The size and the duration of air-carriage of respiratory droplets and droplet-nuclei. Epidemiology & Infection, 44(6), 471-479. https://doi.org/10.1017/S0022172400019288
4. Calmet, H., Inthavong, K., Both, A., Surapaneni, A., Mira, D., Egukitza, B., & Houzeaux, G. (2021). Large eddy simulation of cough jet dynamics, droplet transport, and inhalability over a ten minute exposure. Physics of Fluids, 33(12). https://doi.org/10.1063/5.0072148
5. Vadivukkarasan, M. (2021). A note on the stability characteristics of the respiratory events. European Journal of Mechanics-B/Fluids, 89, 15-20. https://doi.org/10.1016/j.euromechflu.2021.05.001
6. Monroe, K., Yao, Y., Lattanzi, A., Raghav, V., & Capecelatro, J. (2021). Role of pulsatility on particle dispersion in expiratory flows. Physics of Fluids, 33(4). https://doi.org/10.1063/5.0048746
7. Wang, Y., Zhai, C., Cao, Z., & Zhao, T. (2020). Potential application of using vortex ring for personalized ventilation. Indoor Air, 30(6), 1296-1307. https://publons.com/publon/10.1111/ina.12699.
8. Morawska, L., Buonanno, G., Mikszewski, A., & Stabile, L. (2022). The physics of respiratory particle generation, fate in the air, and inhalation. Nature Reviews Physics, 4(11), 723-734. https://doi.org/10.1038/s42254-022-00506-7
9. Bourouiba, L. (2021). The fluid dynamics of disease transmission. Annual Review of Fluid Mechanics, 53(1), 473-508. https://doi.org/10.1146/annurev-fluid-060220-113712

10. Wei, J., & Li, Y. (2017). Human cough as a two-stage jet and its role in particle transport. PloS one, 12(1), e0169235. https://doi.org/10.1371/journal.pone.0169235
11. Li, K., Li, R., Xiao, L., Feng, L., Mu, D., Shi, X., & Gao, N. (2024). Risk assessment of cough droplets in both static and dynamic indoor environments with different ventilation strategies. Building and Environment, 266, 112139. https://doi.org/10.1016/j.buildenv.2024.112139
12. Jiang, J., Wang, H., Lin, J., Wang, F., Liu, Z., Wang, L., ... & Lu, Z. (2025). Nature-inspired hierarchical building materials with low CO2 emission and superior performance. Nature Communications, 16(1), 3018. https://doi.org/10.1038/s41467-025-58339-8
13. Dao, H. T., & Kim, K. S. (2022). Behavior of cough droplets emitted from Covid-19 patient in hospital isolation room with different ventilation configurations. Building and environment, 209, 108649. https://doi.org/10.1016/j.buildenv.2021.108649
14. Behera, S., Bhardwaj, R., & Agrawal, A. (2021). Effect of co-flow on fluid dynamics of a cough jet with implications in spread of COVID-19. Physics of Fluids, 33(10). https://doi.org/10.1063/5.0064104
15. Papoutsakis, A., Danaila, I., Luddens, F., & Gavaises, M. (2022). Droplet nuclei caustic formations in exhaled vortex rings. Scientific reports, 12(1), 3892. https://doi.org/10.1038/s41598-022-07717-z
16. Liu, K., Allahyari, M., Salinas, J. S., Zgheib, N., & Balachandar, S. (2021). Peering inside a cough or sneeze to explain enhanced airborne transmission under dry weather. Scientific Reports, 11(1), 9826. https://doi.org/10.1038/s41598-021-89078-7
17. Hunt, J. C. R., Delfos, R., Eames, I., & Perkins, R. J. (2007). Vortices, complex flows and inertial particles. Flow, turbulence and combustion, 79(3), 207-234. https://doi.org/10.1007/s10494-007-9096-0
18. Ghasemi, A., Roussinova, V., Barron, R. M., & Balachandar, R. (2016). Large eddy simulation of the near-field vortex dynamics in starting square jet transitioning into steady state. Physics of Fluids, 28(8). https://doi.org/10.1063/1.4961199
19. Limbourg, R., & Nedić, J. (2021). An extended model for orifice starting jets. Physics of Fluids, 33(6). https://doi.org/10.1063/5.0048813
20. O'Farrell, C., & Dabiri, J. O. (2014). Pinch-off of non-axisymmetric vortex rings. Journal of fluid mechanics, 740, 61-96. https://doi.org/10.1017/jfm.2013.639
21. Gharib, M., Rambod, E., & Shariff, K. (1998). A universal time scale for vortex ring formation. Journal of Fluid Mechanics, 360, 121-140. https://doi.org/10.1017/S0022112097008410
22. Zheng, H., Gao, L., & Yu, S. C. (2023). Effects of aspect ratio on vortex dynamics in starting rectangular jets. AIAA Journal, 61(10), 4332-4344. https://doi.org/10.2514/1.J062873
23. Akagi, F., Haraga, I., Inage, S. I., & Akiyoshi, K. (2020). Effect of sneezing on the flow around a face shield. Physics of Fluids, 32(12). https://doi.org/10.1063/5.0031150
24. Koullapis, P., Kassinos, S. C., Muela, J., Perez-Segarra, C., Rigola, J., Lehmkuhl, O., Cui, Y., Sommerfeld, M., Elcner, J., Jicha, M., Saveljic, I., Filipovic, N., Lizal, F., & Nicolaou, L. (2018). Regional aerosol deposition in the human airways: The SimInhale benchmark case and a critical assessment of in silico methods. European Journal of Pharmaceutical Sciences, 113, 77-94. https://doi.org/10.1016/j.ejps.2017.09.003.

25. Liu, L., Li, Y., Nielsen, P. V., Wei, J., & Jensen, R. L. (2017). Short - range airborne transmission of expiratory droplets between two people. Indoor air, 27(2), 452-462. https://doi.org/10.1111/ina.12314
26. Aganovic, A., & Cao, G. (2019). Evaluation of airborne contaminant exposure in a single-bed isolation ward equipped with a protected occupied zone ventilation system. Indoor and built environment, 28(8), 1092-1103. https://doi.org/10.1177/1420326X18823048
27. Lu, Y., Oladokun, M., & Lin, Z. (2020). Reducing the exposure risk in hospital wards by applying stratum ventilation system. Building and Environment, 183, 107204. https://doi.org/10.1016/j.buildenv.2020.107204
28. Rudnick, S. N., & Milton, D. K. (2003). Risk of indoor airborne infection transmission estimated from carbon dioxide concentration. Indoor air, 13(3). https://doi.org/10.1034/j.1600-0668.2003.00189.x
29. Zhai, C., Wang, Y., Cao, Z., Zhao, T., Wang, R., Zhang, C., & Wu, S. (2022). Effect of thermal buoyancy on vortex ring air supply mode. Building and Environment, 221, 109257. https://doi.org/10.1016/j.buildenv.2022.109257
30. Abuhegazy, M., Talaat, K., Anderoglu, O., & Poroseva, S. V. (2020). Numerical investigation of aerosol transport in a classroom with relevance to COVID-19. Physics of Fluids, 32(10). https://doi.org/10.1063/5.0029118
31. Wang, H., Li, Z., Zhang, X., Zhu, L., Liu, Y., & Wang, S. (2020). The motion of respiratory droplets produced by coughing. Physics of Fluids, 32(12). https://doi.org/10.1063/5.0033849
32. Sangras, R., Kwon, O. C., & Faeth, G. M. (2002). Self-preserving properties of unsteady round nonbuoyant turbulent starting jets and puffs in still fluids. J. Heat Transfer, 124(3), 460-469. https://doi.org/10.1115/1.1421047
33. Wang, J., Alipour, M., Soligo, G., Roccon, A., De Paoli, M., Picano, F., & Soldati, A. (2021). Short-range exposure to airborne virus transmission and current guidelines. Proceedings of the National Academy of Sciences, 118(37), e2105279118. https://doi.org/10.1073/pnas.2105279118
34. JOHNSON, G. M. (1971). An empirical model of the motion of turbulent vortex rings. AIAA Journal, 9(4), 763-764. https://doi.org/10.2514/3.6273
35. Zhu, J., Zhang, G., Xia, H., Yu, S. C. M., & Gao, L. (2024). The influence of background co-flow on the propulsive characteristics of starting jets. Ocean Engineering, 309, 118473. https://doi.org/10.1016/j.oceaneng.2024.118473
36. Bi, Y., Qin, L., Yu, L., Li, B., Liu, S., & Zuo, Z. (2024). Interactions between a toroidal bubble and a free surface. Journal of Fluid Mechanics, 998, A28. https://doi.org/10.1017/jfm.2024.892
37. Yu, S. C. M., Ai, J. J., Gao, L., & Law, A. W. K. (2008). Vortex formation process of a starting square jet. AIAA journal, 46(1), 223-231. https://doi.org/10.2514/1.29514
38. Yu, S. C. M., Law, A. W. K., & Ai, J. J. (2007). Vortex formation process in gravity-driven starting jets. Experiments in fluids, 42(5), 783-797. https://doi.org/10.1007/s00348-007-0290-6
39. Krueger, P. S., & Gharib, M. (2003). The significance of vortex ring formation to the impulse and thrust of a starting jet. Physics of fluids, 15(5), 1271-1281. https://doi.org/10.1063/1.1564600